RESEARCH ARTICLE

WILEY

Noise simulations of flap devices for wind turbine rotors

Alexandre Suryadi [iD] | Florian Nils Schmidt [iD] | Christina Appel | Nils Reiche |
Roland Ewert | Michaela Herr | Jochen Wild

German Aerospace Center, Institute of
Aerodynamics and Flow Technology,
Braunschweig, Germany

Correspondence
Alexandre Suryadi, German Aerospace Center,
Institute of Aerodynamics and Flow
Technology, Lilienthalplatz 7, 38108
Braunschweig, Germany.
Email: alexandre.suryadi@dlr.de

Abstract

The rotor of a large diameter wind turbine experiences more substantial and more dynamic loads due to the fluctuating and heterogeneous wind field. The project *SmartBlades 2.0* investigated rotor blade design concepts that alleviate aerodynamic loading using active and passive mechanisms. The present work evaluates the acoustics of the two load alleviating concepts separately, an inboard slat and an outboard flap, using the Fast Random Particle Mesh/Fast Multipole Code for Acoustic Shielding (FRPM/FMCAS) numerical prediction toolchain developed at DLR with input from the averaged flow field from RANS. The numerical tools produce a comparable flap side-edge noise spectrum with that of the measurement conducted in the Acoustic Wind Tunnel Braunschweig (AWB). The validated FRPM/FMCAS was then used to analyze the self-noise from a slat at the inboard section of a rotor blade with a 44.45 m radius and compared with that from the outboard trailing edge. Furthermore, the rotational effect of the rotor was included in the post-processing to emulate the noise observed at ground level. The findings show an increase in the slat's overall sound pressure level and a maximum radiation upwind of the wind turbine for the case with the largest wind speed that represents the off-design condition. In operational conditions, the slat adds at most 2 dB to the overall sound pressure level. The toolchain evaluates wind turbine noise with conventional or unconventional blade design, and the problem can be scaled up for a full-scale analysis. As such, the tools presented can be used to design low-noise wind turbines efficiently.

KEYWORDS
numerical, wind turbine noise

1 | INTRODUCTION

Wind turbine development is trending towards larger rotor diameters. With a large rotor, the turbine generates more power. However, it will also experience an increased aerodynamic load. One of the well-established systems for wind turbine control is the blade pitch control. Controlling the blade's pitch angle avoids excessive loads on the blades and increases the lifespan of the wind turbine.[1] However, with large rotors, the scale of the problem increases, for example, the large difference of wind speed between the hub and the tip of the blade, and because of this local controls are appealing. Concepts for local load control are investigated in the project *SmartBlades 2.0*, the acoustic performance of two of which are explored numerically in this paper: (i) an active trailing edge at the outboard rotor and (ii) a rigid slat at the inboard rotor.

Numerical prediction of wind turbine noise using empirical means have been conducted in the past.[2–4] Trailing-edge noise spectrum were calculated based on the empirical BPM (Brooks, Pope, and Marcolini) model[5] for specific segments of the rotor, and accounting for the rotational effects, propagated the far-field noise to the ground. These methods allow for the fast and accurate prediction of wind turbine noise and planning for wind farms. The BPM model exclusively calculates the trailing-edge noise, hence, is inadequate for predicting flap side-edge noise and slat noise generated by the active trailing edge and rigid slat, respectively. In this paper, a numerical procedure based on a coupled fluid and acoustic simulation is presented to calculate the noise sources from various edge sources. The fluid simulation is a Reynolds-averaged Navier–Stokes (RANS) solver, whereas the acoustic simulation consists of the Fast Random Particle Mesh (FRPM) method to generate a turbulence spectrum and the Fast Multipole Code for Acoustic Shielding (FMCAS) to propagate the sound sources to the far field.

The present research article begins with a description of the numerical procedure used to analyze the acoustic performance of the rotor blade devices (see Section 2). This is followed by a validation of the numerical procedure in Section 3, where the FRPM/FMCAS was used to predict the flap side-edge noise and was compared to the measurement results of an active trailing edge flap conducted in the Acoustic Wind Tunnel Braunschweig (AWB), located at the German Aerospace Center's (DLR) Braunschweig site. A summary of the measurement setup and the numerical setup are described. In Section 4, the prediction method was applied to predict the noise of a rigid slat at the inboard section of a wind turbine blade. The goal of this study is to rank the slat's self-noise relative to the trailing-edge noise of the outboard blade segment. The setup and the calculation of the inboard slat noise and the outboard trailing-edge noise are described. Afterwards, the sound immission of the blade's root region including the rigid slat and the outboard region is calculated for an arbitrarily positioned ground observer. Finally, a conclusion of the work is drawn in Section 6.

2 | NUMERICAL PROCEDURE

In the following chapter, the numerical procedure is presented, which was used to analyze the acoustic performance of the different wind turbine's rotor blade devices.

A schematic of the numerical procedure is given in Figure 1.

A fluctuating flow field is reconstructed using the FRPM method under the assumption of isotropic turbulence. The local mean flow information from RANS around a noise radiating edge was used to reconstruct the turbulence field. A part of the CFD domain and the local FRPM domain, which will be referred to as *FRPM patch*, are depicted in Figure 1(i). In this example, the radiating edge is the trailing edge. To justify the quality of the reconstructed turbulence the FRPM generated enstrophy, ζ_{FRPM}, is compared against its ideal (isotropic) counterpart, ζ (not shown in Figure 1). The FPRM procedure is summarized in Section 2.1. The spectral field of the vorticity-induced velocity, $\hat{u}_{n,ic}$, on the surface that intersects with the FRPM patch is exemplified in Figure 1(ii).[*] The spectral field $\hat{u}_{n,ic}$ functions as a sound source in FMCAS as described in Section 2.2. Finally, FMCAS propagates the sound source close to the body on a radial interface centered around the radiating edge, as shown in Figure 1 (iii) by solving the Helmholtz equation using the Boundary Element Method.[6] From the result, the sound pressure level and directivity are evaluated; see Figure 1(iv).

A summary of the FRPM/FMCAS simulation that is relevant for the present study is given below. For a complete description, the authors suggest previous studies.[7–10]

2.1 | FRPM method

In the present simulation, turbulence fluctuation is expressed as the vorticity vector, ω', generated from the averaged variables produced by RANS, namely the turbulent enstrophy, ζ. Mathematically, the turbulent enstrophy is the scalar product of ω' with itself. Its value changes due to the local strain rate of the flow and due to the dissipation by viscous forces. The turbulent enstrophy is expressed in Gorski and Bernard,[11] in tensorial notation denoting the respective vectorial components, as

$$\zeta = \frac{1}{2}\langle\omega_i'\omega_i'\rangle = \frac{\epsilon}{\nu} - \frac{\delta^2 k_t}{\delta x_i \delta x_j} + \epsilon_{ijk}\frac{d}{dx_i}\langle u_j'\omega_k'\rangle, \quad (1)$$

where ϵ, ν, k_t, and u' are the turbulence decay rate, kinematic viscosity, turbulent kinetic energy, and the fluctuating velocity, respectively, and the operator $\langle...\rangle$ denotes the ensemble averaging. The second and third terms in the right-hand side are assumed negligible. Hence, the numerical enstrophy is defined by the turbulence decay rate and kinematic viscosity.

---

[*]$\hat{u}_{n,ic}$ is a complex variable, for illustration only the real part is visualized.
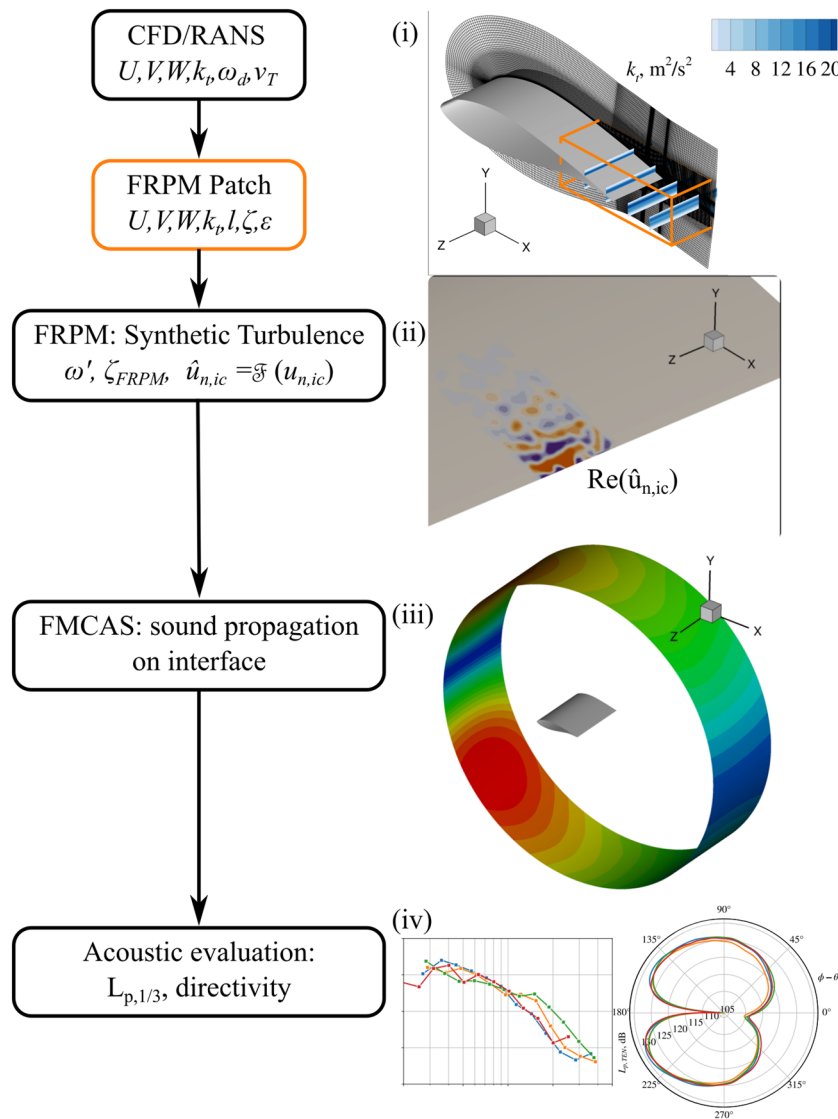
FIGURE 1   Numerical process of the FRPM/FMCAS numerical procedure used in this study. An example of the trailing-edge noise is given. U, V, W: Reynolds-averaged velocity field in x, y, and z, respectively; k_t: turbulent kinetic energy; ω_d: specific turbulent dissipation rate; ν_T: turbulent viscosity; l: turbulent length scale; ζ: turbulent enstrophy; ϵ: turbulent dissipation rate; ω': reconstructed fluctuating vorticity; ζ_{FRPM}: reconstructed enstrophy; $u_{n,ic}$: surface-normal velocity induced by ω'; $L_{p,1/3}$: Third-octave band sound pressure level

The fluctuating vorticity field at $\mathbf{x}$ is expressed spatially using a Gaussian function, $\mathbf{G}(\mathbf{x} - \mathbf{x}')$ and temporally using a white noise function, $\mathbb{U}(\mathbf{x}', t)$, where $\mathbf{x}'$ is an arbitrary point in the flow,

$$\boldsymbol{\omega}'(\mathbf{x}, t) = \nabla \times \left[A(\mathbf{x}) \int_{V_s^n} \mathbf{G}(\mathbf{x} - \mathbf{x}'') \mathbb{U}(\mathbf{x}', t) d^3 \mathbf{x}' \right], \tag{2}$$

where

$$\mathbf{G}(\mathbf{x} - \mathbf{x}') = \frac{1}{l^{3/2}} \exp \left(-\frac{\pi}{2} \frac{|\mathbf{x} - \mathbf{x}'|}{l^2} \right), \tag{3}$$

and

$$l = l(\mathbf{x}) = \frac{c_l}{C_\mu} \frac{\sqrt{k_t(\mathbf{x})}}{\omega_d(\mathbf{x})}, \tag{4}$$

where l is the turbulent length scale, ω_d is the specific turbulence dissipation rate, and $c_l = 0.54$ and $C_\mu = 0.09$ are constants taken from the k-ϵ RANS model.[12] The parameter $A(\mathbf{x})$ is the magnitude of the vorticiy field expressed as

$$A(\mathbf{x}) = \sqrt{\frac{\rho 2l^2}{3\pi} \zeta(\mathbf{x})}, \tag{5}$$

with ρ the density of the transmitive media, which in this study is the density of air at standard atmosphere, $\rho = 1.225 \, \text{kgm}^{-3}$.

In the wavenumber domain, Equation (2) expresses the vorticity fluctuation with a Gaussian spectrum with a length scale, l. In the present simulation, the turbulence is defined as multi-scale problem using a modified Pope spectrum, *Model-3*.[9] The turbulence spectrum is expressed as a superposition of seven vorticity fields, each with a turbulent length scale of l_m:

$$\omega'(\mathbf{x}, t) = \sum_{m=0}^{M=6} \omega'_m(\mathbf{x}, t; l_m). \tag{6}$$

This method allows for the tailoring of enstrophy distribution to specific cases according to the RANS result. In this manner, despite the difference in noise generation mechanism of flap side-edge noise, trailing-edge noise, and slat noise, the methodology treats them in the same way.

Proof of a successful reconstruction of the turbulence field is by recalculating the enstrophy from the reconstructed vorticity, or when $\zeta_{FRPM} = \langle \omega'_i \omega'_i \rangle / 2$ from Equation (2) is an approximate of $\zeta \approx \epsilon / \nu$ from RANS, we consider that the FRPM has reproduced a turbulent field with the same statistical properties.

The FRPM patch is discretized using the following expression:

$$\Delta x = \frac{a_0 Ma}{f_{\max} PPW_{FRPM}}, \tag{7}$$

where Δx is the FRPM characteristic length of the FRPM patch, a_0 is the speed of sound, Ma is the flow Mach number, $f_{\max}$ is the maximum frequency to be resolved, and PPW_{FRPM} is the number of discrete points per wavelength usually taken as 6 points per wavelength.

The parameters required for the FRPM patch are the mean velocity field, the turbulent kinetic energy k_t, mixing length scale $l = \sqrt{k_t / \omega_d}$, the turbulence decay rate $\epsilon = C_\mu k_t / \omega_d$, and turbulence enstrophy $\zeta = \epsilon / \nu$.

2.2 | FMCAS

The FMCAS[6] is a numerical algorithm developed at the Department of Technical Acoustics in DLR-Braunschweig to calculate the sound radiated from a sound source close to a body using the Boundary Element Method. The use of FRPM presented in Section 2.1 coupled with the Boundary Element Method to calculate the far-field noise was proposed and validated in Reiche et al.[10,13]

The Helmholtz equation relates the second-order spatial derivative of the pressure $\hat{p}$ to the sound source $\hat{f}$, where ˆ represents parameters in the frequency domain,

$$(\nabla^2 + k)\hat{p}_x = -\hat{f}; x \in \Omega, \tag{8}$$

which can be solved using the free-field Green's function G_0 integrated over the domain Ω,

$$\hat{p}_{x_o} - \int_{\partial\Omega} \left[\hat{p}_{x_p} \frac{\partial G_0}{\partial n_{x_p}} - G_0 \frac{\partial \hat{p}_{x_p}}{\partial n_{x_p}} \right] d\Omega_{x_p} = \hat{p}_v, \tag{9}$$

the subscripts x_o and x_p indicate an observer's locations and a point on the surface, $\partial\Omega$, respectively. The right-hand side represents a volumetric contribution that does not appear in the problem statement, and thus, it is neglected.

By applying a Neumann boundary condition to Equation (9) on the airfoil's surface, the pressure gradient normal to the surface is

$$\frac{\partial \hat{p}_{x_p}}{\partial n_{x_p}} = Y_{x_p} \hat{p}_{x_p} + V_{x_p}(\hat{u}_n), \tag{10}$$

where Y_{x_p} is the wall admittance and V_{x_p} is the surface excitation that is a function of the wall-normal component of the induced velocity $\hat{u}_n$. The Burton–Miller linear operator B_{x_o} was used to enforce a unique solution of the outer problem of surface $\partial\Omega$ leading to

$$\frac{1}{2}B_{x_o}\hat{p}_{x_o} - \int_{\partial\Omega}\left[\hat{p}_{x_p}\frac{\partial}{\partial n_{x_p}} - Y_{x_p}\right]B_{x_o}G_0\mathrm{d}\Omega_{x_p} = \int_{\partial\Omega}V_{x_p}(\hat{u}_n)B_{x_o}G_0\mathrm{d}\Omega_{x_p},$$

(11)

by substituting Equation (10) to Equation (9). Turbulence interaction with the surface is established by coupling the acoustic velocity, $\hat{u}_{n,a}$, and the incompressible velocity, $\hat{u}_{n,ic}$, or $\hat{u}_n = \hat{u}_{n,a} = \hat{u}_{n,ic}$. The incompressible velocity $\hat{u}_{n,ic}$ is induced by turbulence vorticity ω' provided by Equation (2),

$$\hat{u}_{n,ic} = \mathfrak{F}(\mathbf{n}\cdot(\nabla\times\boldsymbol{\psi}')); \nabla^2\boldsymbol{\psi}' = -\boldsymbol{\omega}'.$$

(12)

Here, $\mathfrak{F}$ indicates the Fourier transform, $\mathbf{n}$ is the wall-normal unit vector, and $\boldsymbol{\psi}'$ is the source potential function. The turbulence vorticity ω' is synthesized using FRPM as described in Section 2.1.

The discretization of the surface is expressed as

$$\Delta x = \frac{a_0}{f_{\max}PPW_{FMCAS}},$$

(13)

where Δx is the surface cell's characteristic length and PPW_{FMCAS} is the number of discrete points per wavelength usually taken as 6 points per wavelength.

One FMCAS simulation computes the sound pressure level at a given frequency for a narrowband spectrum, which will be converted to a one-third octave band when comparing with measurements. Conventionally, the conversion requires the integration of the power spectral density with respect to the narrow bandwidth. This requires the computation of the narrowband sound pressure level over a broad frequency range. To further fasten the numerical process, the integration is avoided by expressing the one-third octave band sound pressure level as

$$L_{p,1/3}(f_c) = 10\log_{10}\left(\frac{\mathrm{d}p_{rms}'^2(f_c)}{(20\mu\mathrm{Pa})^2}\right),$$

(14)

with

$$\mathrm{d}p_{rms}'^2(f_c) = \Phi_{pp}(f_c)f_c\frac{\ln 2}{3} = \Phi_{pp}(f_c)\partial fi\frac{\ln 2}{3},$$

(15)

where $\Phi_{pp}(f_c)$ is the power spectral density at f_c, $\Phi_{pp}(f_c)\partial f$ is the narrowband sound pressure level calculated by FMCAS, and $i = f_c/\partial f$. Hence, a smaller set of FMCAS simulations calculates the sound pressure level at or near the one-third octave center frequencies.

3 | ACTIVE TRAILING EDGE

In this section, the investigation of an active trailing edge device is presented to validate the numerical procedure given in Section 2. The validation is supported by measurement results conducted in the AWB. The measurements are summarized in the following subsection.

3.1 | Measurement setup

Acoustic measurements of the active trailing edge using a blade section model with a DU08-W-180 cross-sectional profile, a chord length of 0.3 m and a span length 1.2 m and depicted in Figure 2.[14] The blade model is equipped with a plain flap that has a chord length of 0.09 m and a span length of 0.4 m at the mid-span section; see also Figure 3. Turbulent boundary layer transition was forced by means of a zigzag shaped, boundary layer tripping device with a height of 0.205 mm positioned from the leading edge at the 5% and 10% chord length on the suction and pressure side, respectively. Measurements were conducted at wind speeds of 40, 50, and 60 m/s, which corresponds to the chord length based Reynolds numbers of 800,000, 1,000,000, and 1,200,000, respectively. The sound radiation was measured with the blade section model set to three angles of attack and flap deflection angles between $-5°$ to $5°$ with increments of $1°$ and $-10°$ and $10°$. Far-field noise was measured using
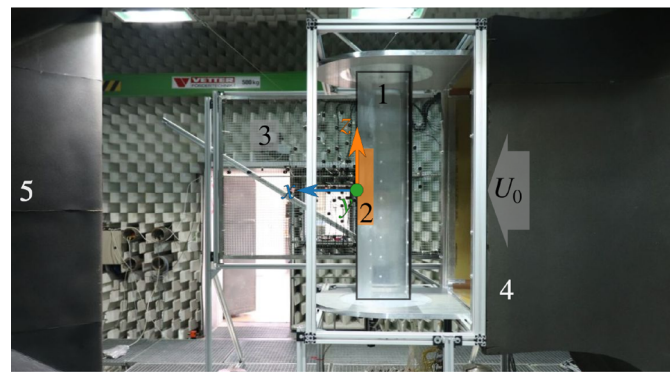
1: Blade section model 2: Plain flap 3: Microphone array
4: Wind tunnel nozzle 5: Wind tunnel collector

FIGURE 2 Experimental setup in the AWB. The pressure side of the blade section model is facing the reader
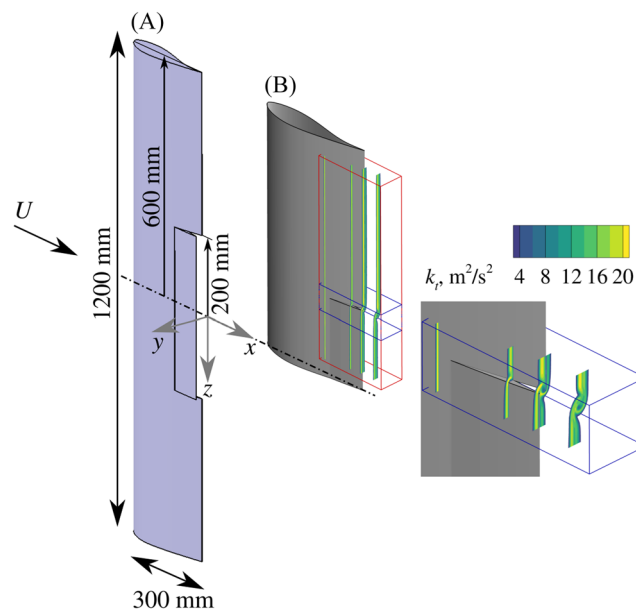

FIGURE 3 (A) The schematic of the blade model, with negative flap angle deflection, used in the measurement and (B) the RANS simulated flow field in the FRPM patch around the trailing edge (framed in red) and around the flap side edge (framed in blue). Profiles of the turbulent kinetic energy k_t illustrates the flap side-edge vortex

a 1 m diameter phased array consisting of 96 1/4-inch microphones facing the suction and pressure sides of the blade section model. The suction and pressure side facing acoustic measurements are independent of each other. The sound map and power spectrum were realized using the deconvolution algorithm CLEAN-SC.[15] CLEAN-SC allows for separating sound sources outside the area of integration. Hence, the effect of sound sources other than the trailing-edge noise and flap side edge noise are minimized.

Due to the flap's small size, the noise sources' significance is judged by the noise reduction effects of materials that inhibit noise radiation. Namely, porous material was used to substitute the solid flap side edges to reduce flap side-edge noise, whereas the trailing-edge brush was added to the trailing edge to reduce trailing-edge noise. A porous material as a mean for noise reduction has been investigated thoroughly, for example, in previous studies.[16–18] The noise reduction potential for trailing-edge brush was investigated in Herr[19] and Suryadi et al.[20] The sound pressure levels with the noise reduction material are compared with the reference solid edges to understand the significance of each noise source. A key point in the measurement is that the flap side-edge noise is not a significant noise source when the flap deflection angle is between $-5°$ and $5°$. It becomes a significant noise source when the deflection angle is $-10°$ or $10°$. The flap side-edge noise of the solid side edge will be used for validation of the numerical results.

3.2 | Numerical setup

Three-dimensional simulations were carried out to reproduce the flow field around the flap side edge. A sketch of the blade section model in experiments and in the simulations are shown in Figure 3 with the center of coordinate's origin at the trailing edge's mid-span at zero flap deflection. The numerical spatial discretization model consists of the half-span of the experimental model. The numerical domain has a far field extending to 100 chord lengths. The mid-span of the model has a symmetrical boundary condition, whereas on the opposite side the wall boundary condition is used to reflect the support walls in the experiment; see Figure 2. For accurate representation of the boundary layer the initial cell height next to the blade's surface is $y^+ < 1$ and the growth ratio in the wall-normal direction is 1.1. Overall, the mesh contains approximately 30×10^6 cells. The simulations were carried out using the coupled implicit solver with a second-order discretization in Star CCM+ and k-ω SST turbulence model was selected, because it provides the necessary parameters for the aeroacoustic analysis.[14] The turbulent kinetic energy distribution, k_t, around the flap side edge is shown in Figure 3B as a result of the sudden change of the profile introduced by the deflected flap.

The pressure coefficient from RANS is compared with the one measured in the AWB in Figure 4. The wind tunnel model in the AWB is set to an angle of $\alpha_g = 5°$ to the free stream, this is an uncorrected angle of attack because of the deflection of the wind tunnel's jet because of the surface curvature of the model. This angle is equivalent to an angle of attack of $\alpha = 0°$ for a infinite domain.

The turbulence reconstruction from RANS is localized to two volumes, *FRPM patches*, around the radiating edge. The two patches are a wide span encompassing the trailing edge and flap side edge and a narrow span one encompassing the flap side edge. The size of the first volume is $0.192\,\text{m} \times 0.064\,\text{m} \times 0.512\,\text{m}$ in the direction along x, y, and z. The spanwise length of this patch was chosen so that secondary flow structures due to the wall are not included. The size of the volume around the flap side edge is $0.192\,\text{m} \times 0.064\,\text{m} \times 0.064\,\text{m}$. Both volumes have a cell size of $0.002\,\text{m}$, such that the maximum frequency that FRPM can resolve is $f_{max} \approx 8\,\text{kHz}$. Both patches are shown in Figure 3B.

A spatial smoothing function with a Gaussian kernel is introduced to the FRPM input parameters to ensure smoothly distributed derivatives. Special care was taken to maintain zero values inside the solid. Another kernel is introduced in the FRPM patch to ensure that vorticities gradually gain or lose their energy when entering or leaving the patch, which is accomplished by introducing a $\cos^2$ ramp function at the sides of the volumetric patch.

3.3 | FRPM turbulence reconstruction

The reconstructed enstrophy from FRPM, as described in Section 2.1, is shown in Figure 5 for a cross-section of the trailing edge at $z = -0.4\,\text{m}$ and of the flap side-edge region at $z = -0.2\,\text{m}$. Overall, the reconstructed turbulence enstrophy, ζ_{FRPM}, approximates the target enstrophy, ζ, sufficiently well. The target enstrophy field and other turbulent parameters from RANS are the results of the integration of their respective turbulence spectrum from $k \rightarrow 0$ to the Kolmogorov scale wavenumber. The FRPM reconstructed field has a limited integration range, with the lower limit depends on the domain size and the upper limit on the cell size. The loss of spatial resolution is accounted for by tailoring the spectral content to the range of resolvable wavenumbers introduced in Rautmann[21] and applied in Wohlbrandt et al[22] and Reiche et al.[23]
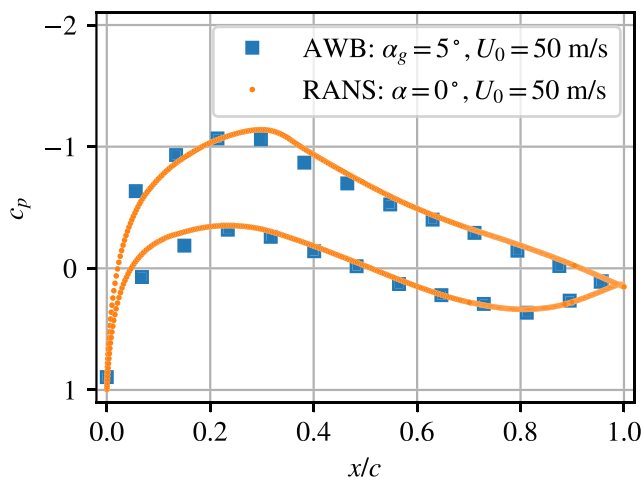

FIGURE 4 Pressure coefficient of the trailing edge between the measurement in the AWB and RANS. The uncorrected wind tunnel angle is $\alpha_g = 5°$, which is equivalent to the angle of attack $\alpha = 5°$ in the numerical domain
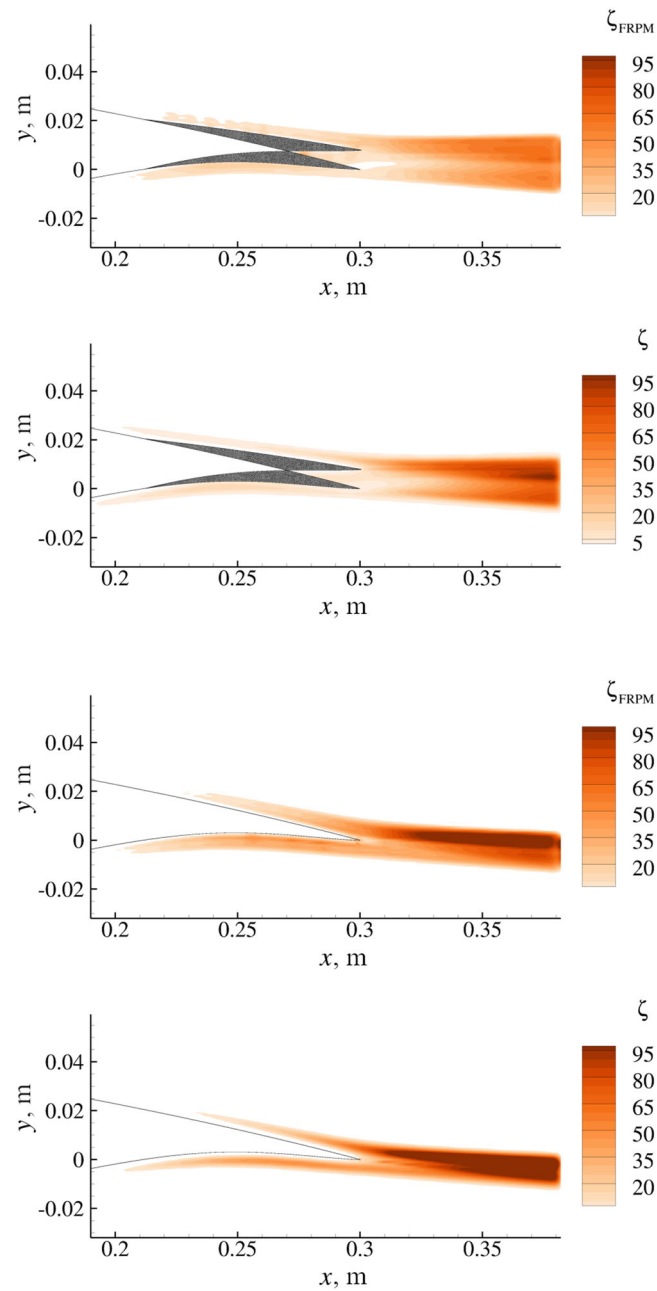
FIGURE 5 Non-dimensional enstrophy reconstructed using FRPM, ζ_{FRPM}, in comparison with the analytical enstrophy, ζ, from the patch illustrated in Figure 3: (A) cross-section of the flap side edge at $z = -0.2$ m and (B) the trailing edge at $z = -0.4$ m

3.4 | FMCAS result

Figure 6 is a comparison between the sound pressure level spectra between the experiment and the simulation for the wider FRPM patch. The sound pressure level is referenced to an observer at 1 m from the trailing edge and directly below it, and to a line source of 1 m in length. Because of the simulation's stochastic method, the numerical prediction produced a sound spectrum within a margin of error from the 20:1 confidence interval (dashed line in Figure 6), comparable to that of the experiments shown by the markers with a ± 1 dB margin of error from the measurement system.

As described in Equation (2), the fluctuating turbulence field is generated using a convolution integral of a white noise field and a spatial Gaussian filter kernel. A reliable average in this study was obtained by repeating the simulation 15 times by realizing a different white noise field each time. Each realization of the FRPM/FMCAS simulation of the trailing-edge region is shown as the light-blue line with round markers in Figure 7. The ensemble averages of every 5, 10, and 15 realizations and the upper and lower bounds of the ensemble average of 15 realizations
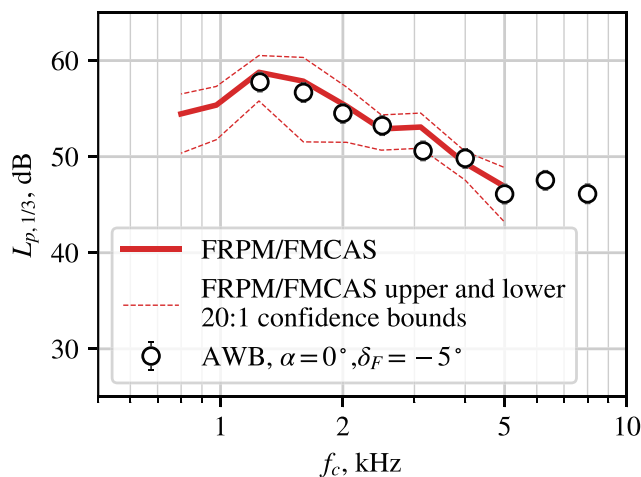
FIGURE 6 A comparison of the far-field sound pressure level between experiments and simulation
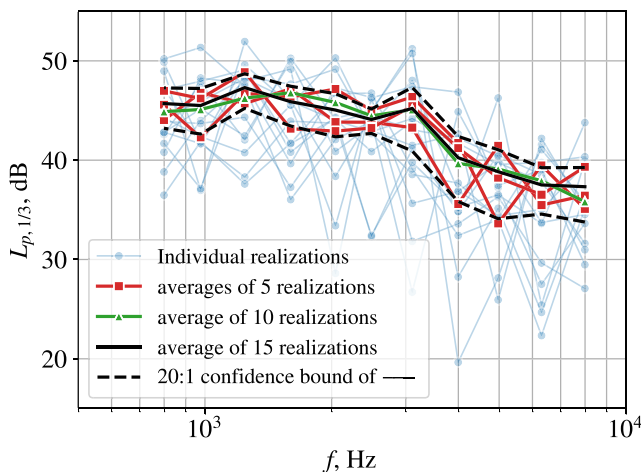

FIGURE 7 Stochasticity of the sound pressure level as a result of the random particle method
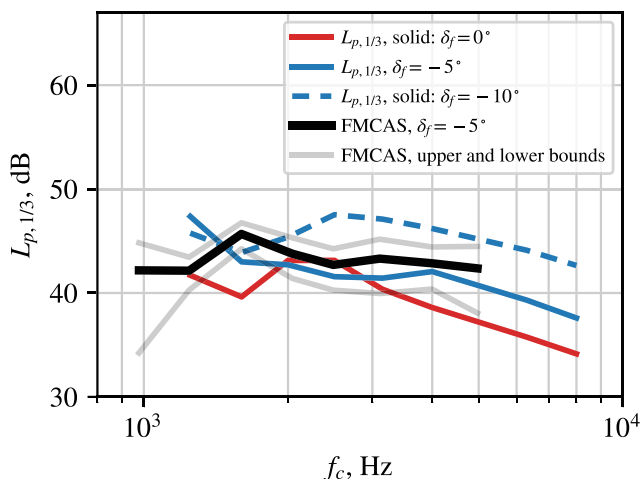

FIGURE 8 A comparison of the far-field sound pressure level of the flap side-edge noise between experiments and simulation using the narrow FRPM patch

with a 20:1 confidence are shown in Figure 7. The upper and lower confidence bounds are approximately $+1.5$ and -3 dB, respectively. At least 10 realizations are required to make a smooth averaged spectrum.

The comparison of experimental and numerical sound pressure level spectra in Figure 8 is localized to the flap side edge. Figure 8 shows distinctively the frequency range of the flap side-edge noise $f_c > 2.5$ kHz for $\delta_f = -5°$ and $f_c > 2$ kHz for $\delta_f = -10°$, which is consistent with Brooks T., Humphreys,[24] where the flap side-edge noise scales with the characteristic radius of the flap side-edge vortex.

4 | RIGID INBOARD SLAT

In the following section, the acoustic performance of a rotor blade geometry of the wind turbine S88 with a rigid slat is analyzed. The rigid slat will be installed and tested on a Suzlon S88 wind turbine, S88-2.25 MW, in Rajasthan, India. Since the main goal of the project *SmartBlades 2.0* is the alleviation of the blade's aerodynamic loading, the measurements will focus on the blade's loads and the wind turbine's power generation with reference to the wind field. The acoustic evaluation was part of the rigid slat design process. This acoustic evaluation was conducted using the FRPM/FMCAS validated in Section 3. The noise of the rigid inboard slat is compared with the trailing-edge noise from the outboard section of the wind turbine's blade, which is the major contributor to wind turbine aeroacoustic.[25]

4.1 | Numerical investigation

The examined rotor blades are geometries from the portfolio of the company Suzlon. The rigid slat was designed in the project SmartBlades 2.0 and is based on the investigations made by Manso Jaume and Wild.[26] In Table 1, the parameters of the investigated geometry are presented.[27]

The wind turbine's rotor blades in combination with the designed rigid slat are shown in Figure 9. One of the rotor blades is colored in green including the rigid slat colored in blue. The pressure side of the blade is facing upwind. The main blade element's trailing edge is highlighted in red, and its leading edge is in purple. The rotor's rotational velocity vector is along the x-direction $\boldsymbol{\Omega} = \Omega \hat{e}_x$ and the wind speed is $\mathbf{U} = U_0 \hat{e}_x$.

In the three-dimensional flow simulations, the three rotor blades including the designed rigid slats were considered as an isolated geometry. Accordingly, the nacelle and the turbine tower were neglected in the studies. The surface of each rotor blade and the surface of each slat were meshed with ordered triangles, which were extruded as prism layers. The resolution of the boundary layer is obtained by 32 cells in the region normal to the wall. Hereby, the rotor blade and the slat were meshed with an O-topology with a first wall spacing that reaches the condition $y^+ \approx 1$. The prism layers are followed by tetrahedra, with which the entire far field is meshed. The far field is designed cylindrical with a length of $20\mathbb{R}$ and a radius of $10\mathbb{R}$. The whole computational grid of the three blades including its rigid slats consist of approximately 107 million points.

As mentioned before, the numerical investigations were made with the use of steady-state RANS simulations. The flow solver is the DLR TAU code,[28] which is an unstructured finite-volume vertex-based CFD solver. The RANS simulations were run with the k-ω-SST turbulence model. The flow can be assumed incompressible because the tip Mach number is approximately 0.23. The boundary layer of the rotor blades as well as the slats was assumed to be fully turbulent. The inflow was defined as uniform with a turbulence intensity of $Tu_0 = 0.001$ at the far-field boundary. This is an idealized ambient condition for the wind turbine to provide a common framework between different cases to establish an acoustic prediction toolchain for evaluating the additional noise from the new blade elements, such as the plain flap in Section 3 or the rigid slat discussed in this section. The simulations were run for different wind speeds, whereby a fixed rotational speed and a fixed rotor pitch angle were set with reference to a control strategy designed by Suzlon. The parameters used in the numerical studies are listed in Table 2.

The 1 m span localized blade sections to be acoustically simulated are shown in Figure 9 and will be represented by the radial cross-section of their mid-spans, R. The mid-span profiles are shown in Figure 10. At $R = 10$ m, the slat's chord length is $c_s = 0.52$ m, and at $R = 36$ m, the outboard profile's chord length is $c_r = 1.428$ m. The blade and boundary layer parameters at R is tabulated in Table 2. In the design, the slat is attached to the blade by two support structures at $R = 4.25$ m and $R = 9.75$ m. These supports are not modeled in the simulation. Hence, the resulting flow field is not affected by them. The acoustic analysis is centered on the slat's trailing edge at 9.5 m $\leq R \leq 10.5$ m and the blade's trailing edge at 35.5 m $\leq R \leq 36.5$ m. Four wind speeds are defined for the simulation $U_0 = 4, 6, 9,$ and 16 m/s. The blade is also designed with a local twist angle θ_{tw}, such that the angle that the chord line makes with the y-axis is $\theta = \theta_p + \theta_{tw}$. Additionally, relative to the blade's chord line, the slat's

TABLE 1 Parameters of the investigated geometry of the Suzlon S88-2.25 MW rotor blade and the designed rigid slat

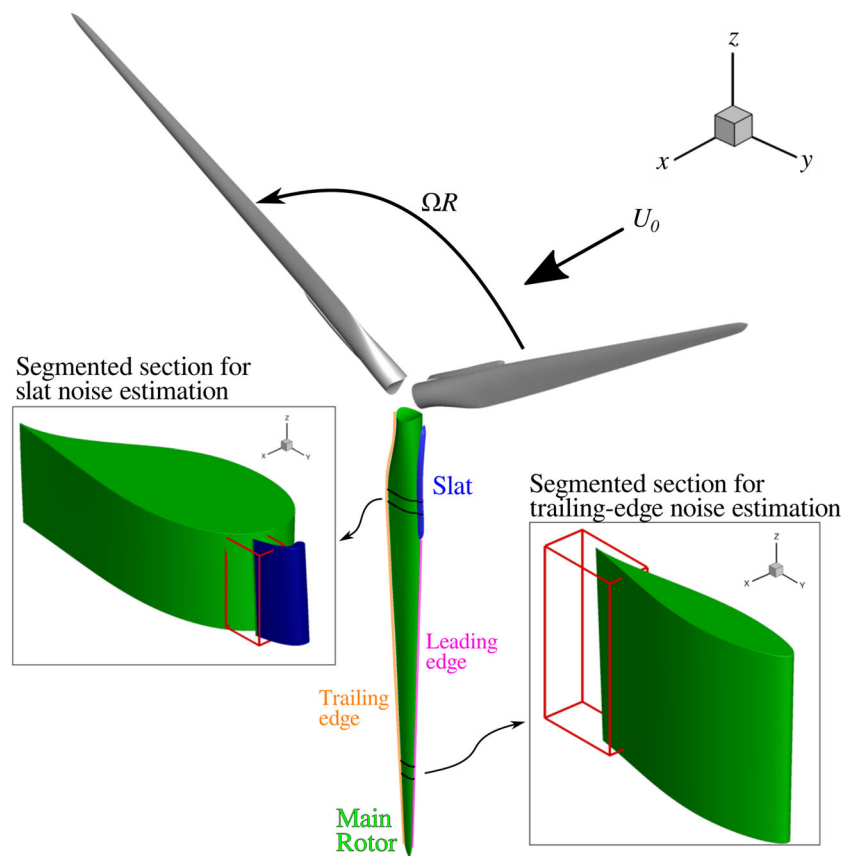|	
Rated power (kW)	2250
Rated wind velocity (m/s)	12
Blade radius (m)	44.45
Slat length (m)	11
Slat mean chord length (m)	0.52

FIGURE 9 A sketch of the Suzlon S88 wind turbine excluding its tower and nacelle. Segments of the blade and FRPM patches (framed in red) for the slat noise and trailing-edge noise estimation are shown in the inset. The FRPM patches enclose the flow information at $R = 10 \pm 0.5$ m for the slat noise and $R = 36 \pm 0.5$ m for the trailing-edge noise

TABLE 2 R: radial position of the blade section (m), U_0: wind speed (m/s), Ω: rotational speed (RPM), θ_p: local pitch angle (°), θ_{tw}: local twist angle (°), θ: blade angle (°), $U_{0,l}$: local inflow velocity (m/s), δ_0: boundary layer thickness (mm), δ_1: boundary layer displacement thickness (mm), and $Re = c_i U_{0,l}/\nu$ is the chord-based Reynolds number of the respective segment, where the subscript i represents the parameters s and r, as illustrated in Figure 10

R	U_0	Ω	θ_p	θ_{tw}	θ	$U_{0,l}$	δ_0	δ_1	Re_c
10	4	11.78	1.5	10.77	20.73	12.90	43	33.23	456,000
	6	12.30	0	10.77	19.23	14.06	40	33.46	497,000
	9	15.32	−1.5	10.77	17.73	18.12	65	43.73	641,000
	16	16.23	11.65	10.77	30.83	22.39	133	57.92	792,000
36	4	11.78	1.5	1.29	2.79	44.57	40	10.34	4,330,000
	6	12.30	0	1.29	1.29	46.71	45	14.04	4,538,000
	9	15.32	−1.5	1.29	0.21	58.37	55	19.22	5,670,000
	16	16.23	11.65	1.29	12.94	63.01	40	10.34	6,121,000

chord line has an initial angle of $8.46°$. The local inflow velocity vector along the x- and y-direction is defined as $\mathbf{U}_{0,l} = U_0(1-a)\hat{e}_x + \Omega R(1+a')\hat{e}_y$, where $a = 0.33$ is the axial induction factor and $a' = (1-3a)/(4a-1)$ is the tangential induction factor, and the magnitude of $\mathbf{U}_{0,l}$ is defined as $U_{0,l}$.

FRPM assumes a stationary model in a steady flow; hence, the RANS field has to be transformed to a coordinate system moving with the blade. The velocity relative to the moving blade $U = U^*$, $V = V^* - \Omega R \cos(\arctan(y/z))$ and $W = W^* + \Omega R \sin(\arctan(y/z))$ with U^*, V^*, and W^* are the mean velocity vector components relative to a stationary observer in x-, y-, and z-directions, respectively. The flow streamlines, pressure coefficients of the two blade sections in Table 2, and the slat's skin friction coefficient are shown in Figures 11–13, respectively. The pressure coefficient is $c_p = (P_s - P)/(0.5\rho U_{0,l}^2)^2$, where P_s and P are the steady-state static pressure on the surface and the ambient pressure, respectively.
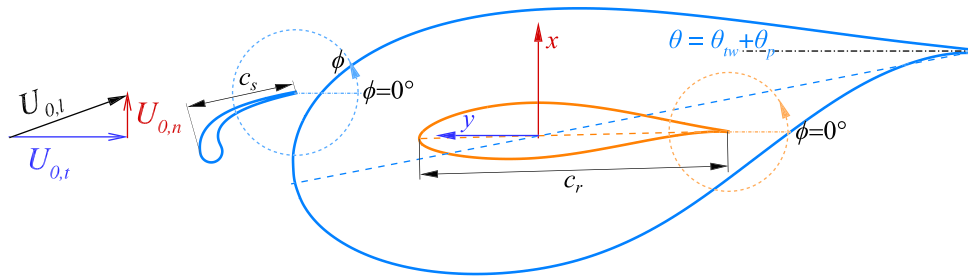
FIGURE 10 The slat, the inboard, $R = 10$ m, and the outboard, $R = 36$ m, sections of the blade
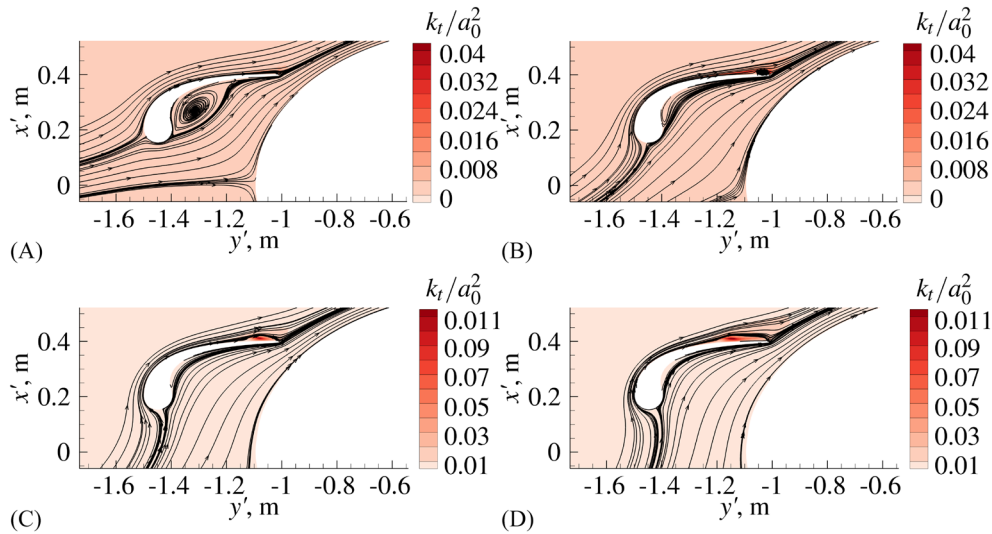

FIGURE 11 Cross-sectional views of the three-dimensional flow field around the slat at $R = 10$ m and its two-dimensional streamlines. (A) $U_0 = 4$ m/s, (B) $U_0 = 6$ m/s, (C) $U_0 = 9$ m/s, and (D) $U_0 = 16$ m/s

The color contour in these figures represents the turbulence kinetic energy normalized with the square of the speed of sound. The coordinates in Figures 11 and 12 are x' and y' which are the spatial coordinates x, y rotated by θ given in Table 2. The streamlines around the slat show two regions with a flow separation bubble. First, the region around the bend on the pressure side exhibits what is commonly known as a cove vortex, which shrinks with larger angles of attack. The second region is on the slat's suction side, which grows with larger angles of attack. The effect of a flow separation bubble is a local minimum of c_f as shown in Figure 13C. In Figure 13B, the flow separation bubble appears to accelerate the flow, but this can be attributed as an artifact of the k-ω-SST model.

The streamlines at the outboard blade section show the change of the stagnation point position due to the change of the angle of attack. Most notable is at $U_0 = 16$ m/s, where the pitch angle change results in a decrease of the angle of attack. In contrast, at $U_0 = 16$ m/s, the slat's angle of attack is increased.

For evaluating noise, there are two regions of interest: (1) the slat trailing edge that is identified as the possible noise source and (2) the outboard trailing edge, which is the major contributor to wind turbine noise for an observer on the ground.[29] The size of the FRPM patches of both region is 0.32 m × 0.48 m × 1 m and the cell size $\Delta x = \Delta y = 0.002$ m and $\Delta z = 0.025$ m, which allow for FRPM to resolve a spectrum with a maximum frequency of 1.1 kHz for the slat trailing region and 3.9 kHz for the outboard trailing edge. The patch has a total of 1,552,040 nodes.

4.2 | FRPM turbulence reconstruction

Figure 14 shows the distribution of enstrophy for $U_0 = 6$ m/s as an example. The FRPM reconstructed enstrophy is consistently smaller than that of the analytical; however, their distribution appears to be consistent with each other. The discrepancy is caused by the blade's size, which requires a larger domain size and smaller cell size. A larger domain size or smaller cell size would reconstruct better the wavenumber range of the turbulence field. The spatial lengths for the active trailing edge are $\ell = (0.002, 0.480)$ m. Despite the discrepancy in terms of level, the sound pressure level spectra follow the appropriate scaling laws, as will be shown in the next section.
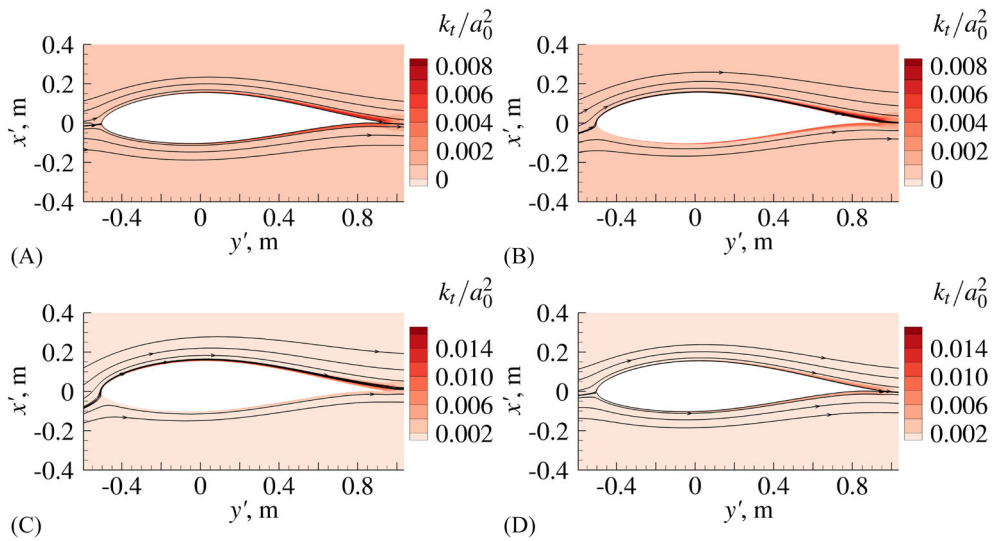
FIGURE 12 Cross-sectional views of the three-dimensional flow field around the outboard blade section at $R = 36$ m and its two-dimensional streamlines. (A) $U_0 = 4$ m/s, (B) $U_0 = 6$ m/s, (C) $U_0 = 9$ m/s, and (D) $U_0 = 16$ m/s
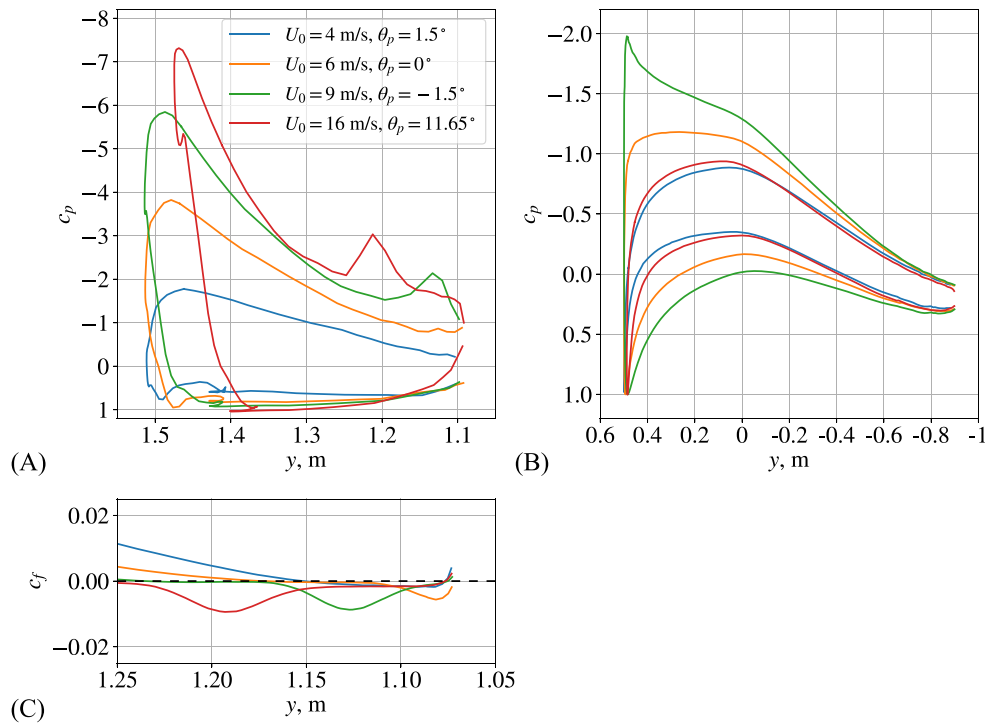

FIGURE 13 Pressure coefficients of the (A) slat and (B) outboard blade section. Only 1 of every 4 datapoints are shown, (C) skin friction coefficient of the downstream half of the slat's suction side

4.3 | FMCAS result

4.3.1 | Outboard trailing edge—Trailing-edge noise

The overall trailing-edge noise directivities, L_p, of the four wind speeds are shown in Figure 15. The overall sound pressure levels are the sum of the sound pressure level spectra between 300 Hz $\leq f_c \leq$ 4000 Hz. The levels are scaled to an observer 1 m away from the trailing edge and to an expected line source of 1 m. In Figure 15B, the overall directivity is in agreement with the trailing-edge noise scaling of $U_{0,l}^5$, see Equation (16), and the directivity angle is corrected with respect to the blade's local pitch angle, that is, $\phi - \theta$.
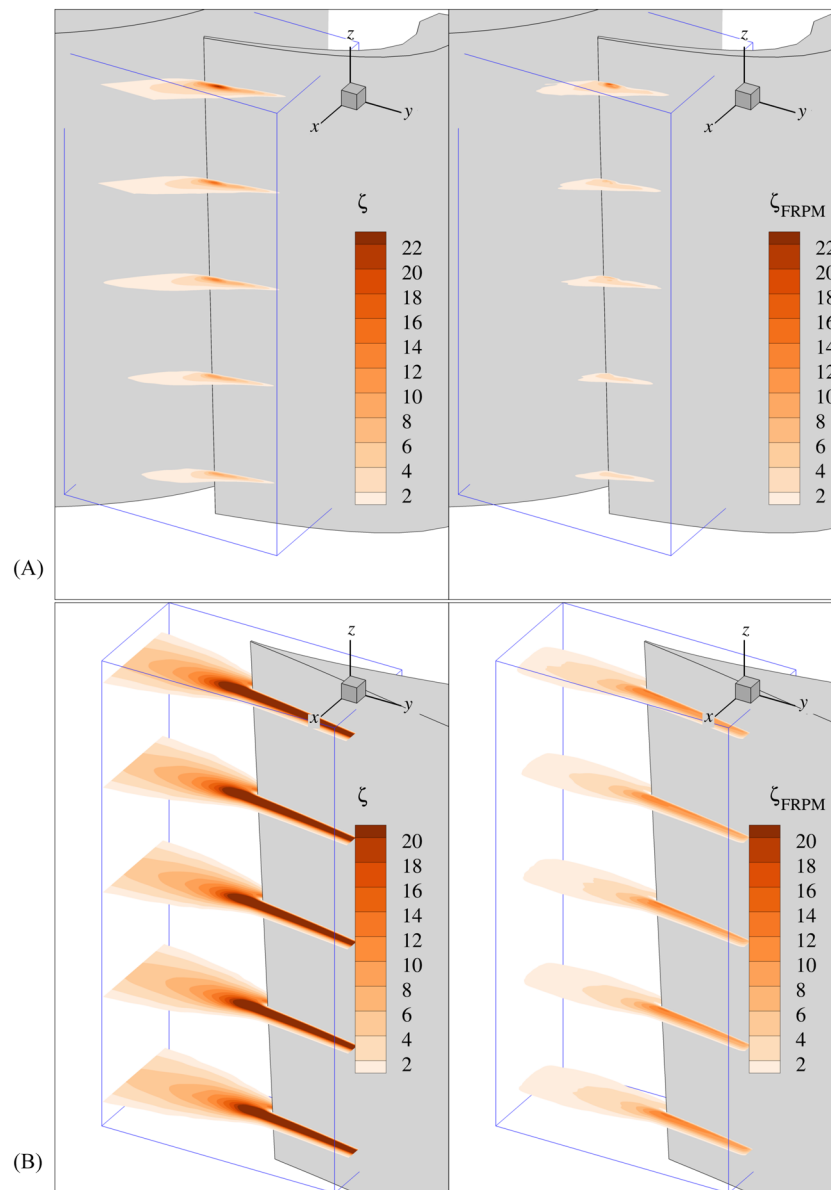
FIGURE 14 Non-dimensional analytical enstrophy, ζ, and reconstructed enstrophy, ζ_{FRPM} for (A) the slat region and (B) outboard trailing edge

$$L_{p;TEN} = L_p - 50\log(U_{0,I}/a_0) - 10\log(\delta_0 b/R_o^2). \tag{16}$$

The third-octave band sound pressure level, $L_{p,1/3}$, in Figure 16 is a sample from Figure 15B at $\phi - \theta = 208°$, which is the one that contributes to the strongest overall sound pressure level. The scaled trailing-edge noise spectra, $L_{p,1/3;TEN}$ expressed in the same manner as Equation (16), scales well for $0.3 < f_c\delta_0/U_{0,I} < 1$. Above the upper range, two spectra with $U_0 = 4$ and $16 \, \text{m/s}$ collapse well, but not for the others. This discrepancy is caused by the trailing-edge noise scaling characterizing the scales in the inertial range. In contrast, the dissipative range is characterized by the viscous length scale and friction velocity. In short, the trailing-edge noise scaling is expected to cover the low-to-medium frequencies but not the high-frequency range. Figures 15 and 16 show that the trailing-edge noise characteristics can be captured by the present simulation tools.

A comparison of FMCAS result using DLR's standard CAA code PIANO (Perturbation Investigation of Aerodynamic NOise) is shown in Figure 17 for the case of $R = 36 \, \text{m}$, $U_0 = 6 \, \text{m/s}$. The far-field noise spectrum from PIANO is shown for the directivity angle of $\phi = 275°$, that is, the observer is at an angle perpendicular to the angle of attack and under the blade section. For a fair comparison, the FMCAS far-field noise spectrum at the same angle is shown in Figure 17 along with $\phi - \theta = 208°$, or $\phi = 208°$. Both spectral levels are referenced to an observer at 1 m away from the sound source and the sound source is an assumed line source with a span of 1 m. The PIANO spectrum plateaus at approximately 55 dB for $f \geq 1 \, \text{kHz}$, whereas the FMCAS result decays further. The peak level of FMCAS is lower than that of PIANO. It should also be noted that
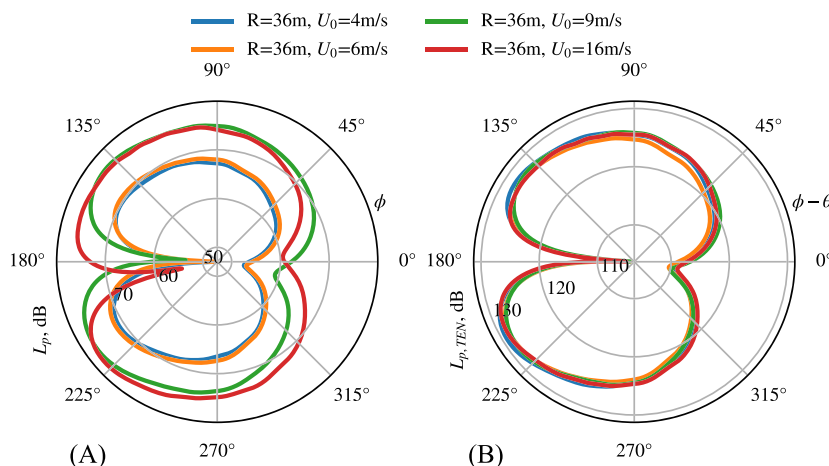
FIGURE 15 Noise directivity of the outboard trailing edge: (A) unscaled and (B) scaled according to Equation (16)
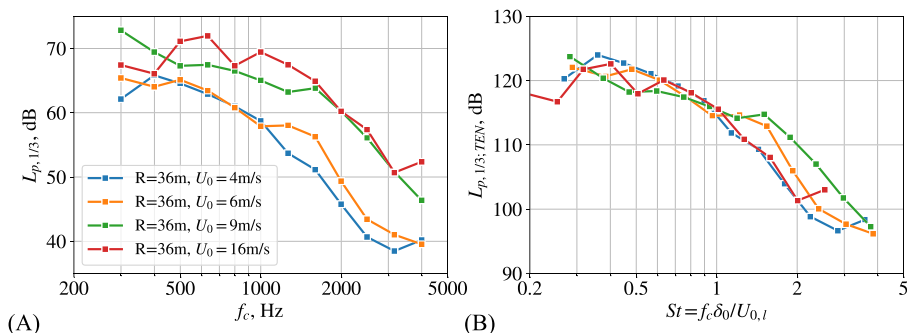

FIGURE 16 Sound pressure level at $\phi - \theta = 208°$ of the outboard trailing edge: (A) unscaled and (B) scaled according to Equation (16)
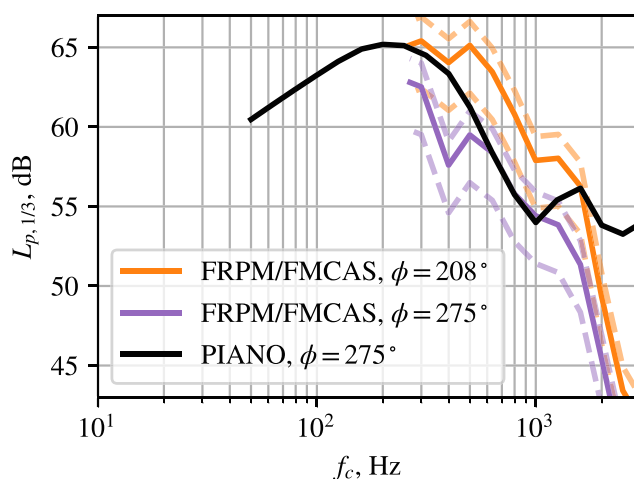

FIGURE 17 Comparison of sound pressure level calculated using PIANO and FRPM/FMCAS. The dashed line is the upper and lower bounds of the 20:1 confidence interval of the simulation

PIANO resolves a two-dimensional problem using a two-dimensional result from RANS as input, whereas FMCAS resolves a three-dimensional problem using a three-dimensional result from RANS as input. In general, FMCAS and PIANO spectra follow the same trend for 300 Hz < f_c < 1000 Hz at $\phi = 275°$. The FMCAS spectrum at $\phi = 208°$ decays in the same way as the spectrum at $\phi = 275°$, but it is 5 dB larger due to the directivity.

The advantage of using FRPM/FMCAS is that, unlike PIANO, the governing equations are resolved only on the boundaries. Hence, a three-dimensional domain can be resolved with fewer computer resources. In total, the FRPM calculation took 4 h and 48 min on an Intel XEON W-2135 3.75 GHz using a single thread, and FMCAS were calculated for each frequency in parallel, taking 5 h and 31 min on a 32 cores AMD EPYC 7601 2.2 GHz. Parallel FRPM is currently under development at DLR. For comparison the two-dimensional PIANO result takes approximately 6 h with 65 CPUs.

4.3.2 | Slat trailing edge—Slat noise

The overall sound pressure level of the unscaled and scaled directivity, calculated using Equation (16), of the slat noise are shown in Figure 18. The slat noise is generated from the flow field exemplified in Figure 11. This directivity is an integral result with limits 100 Hz < f < 600 Hz. The sound pressure levels are scaled to an observer positioned at 1 m from the slat's trailing edge and to an assumed line source with a length of 1 m. The scaling of Equation (16) fits for all cases except $R = 10$ m, $U_0 = 4$ m/s. The reason for this exception is not fully clear. The shape of the directivity of $R = 10$ m, $U_0 = 4$ m/s is similar to the other cases, and only the magnitudes do not follow the scaling argument. The flow field of case $R = 10$ m, $U_0 > 4$ m/s feature a significantly reduced cove vortex but increased separation bubble close to the trailing edge on the suction side, whereas at $R = 10$ m, $U_0 = 4$ m/s the cove vortex is more pronounced; compare Figure 11. These flow characteristics might explain the inconsistency of the applied velocity scaling. Regardless, the maxima of the upper and lower directivity lobes are located at $\phi - \theta = 135°$ and $245°$, respectively, and the maximum levels between the upper and lower lobes have no clear distinction. The proper scaling argument is outside of the scope of this study and will be left as a task for future investigations.

The sound pressure level spectra at four wind speeds are extracted from $\phi - \theta = 135°$ in Figure 18, and they are shown in Figure 19 for both unscaled and scaled levels. The sound pressure level at the negative slope scales with $U_{0,l}^{4.5}$ instead of the fifth power, Equation (17).

$$L_{p,1/3;SN} = L_{p,1/3} - 45 \log(U_{0,l}/a_0) - 10 \log(c_s b/R_o^2). \tag{17}$$

This scaling follows the typical slat noise scaling[30] and is different from the scaling applied to the overall sound pressure level directivity. The difference can be due to the simulation's low spectral resolution, which has a frequency width of $\Delta f \approx 133$ Hz and the narrow spectral range not containing enough energy to capture the same scaling. Nevertheless, the position of the maxima of the directivity lobes is unaffected by the scaling method. It is dependent only on the geometry, as shown by the directivity pattern collapsing together with the directional angles $\phi - \theta$. From here, it can be concluded that the present simulation tools can capture the slat noise characteristics well.

5 | DISCUSSION

The wind turbine noise is predicted based on the spectral results described in Section 4 using a new, simple and fast, prediction method described in Appel et al.[31] The prediction method treats each blade in the same ideal ambient condition for direct comparison of different rotor
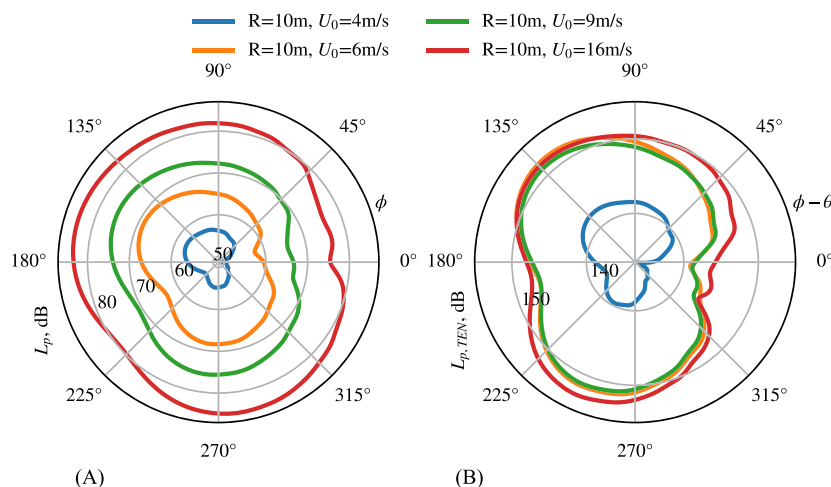

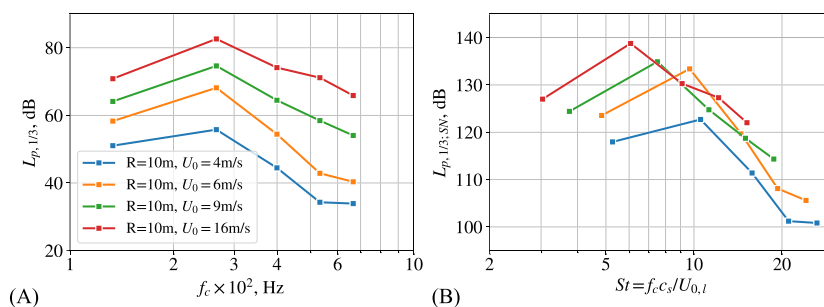**FIGURE 18** Slat noise directivity: (A) unscaled and (B) scaled according to Equation (16)

FIGURE 19 Slat noise sound pressure level at $\phi - \theta = 135°$: (A) unscaled and (B) scaled according to Equation (17)
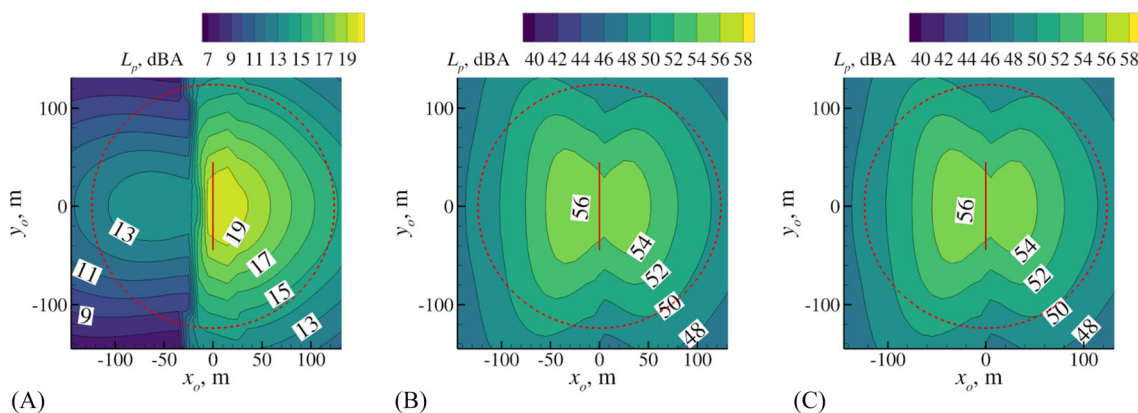

FIGURE 20 With $U_0 = 4$ m/s, the noise footprint for one revolution from (A) slat, (B) outboard trailing edge, and (C) combination of both

configurations or concept studies. The sound spectra at various conditions due to the blade's revolution are emulated from the input spectra. The acoustic impact on the ground is a superposition of the sound source from each blade element. In the present study, only two segments are available. Hence, the final acoustic level is not representative of a rotor blade at full length. This exercise aims to rank the level of slat noise and outboard trailing-edge noise at an arbitrary ground position.

The A-rated overall sound pressure level as experienced by an observer on the ground at a position x_o, y_o is mapped in Figures 20–23 for wind speeds of $U_0 = 4$ to 16 m/s, respectively. The sound maps in these figures are the average over a revolution of the rotor blades. In (A), the sound map is explicitly the result of the slat noise, and in (B), it is the result of the outboard trailing-edge noise. In (C), the sound map is the result of the superposition of both noise sources. The red vertical line represents the rotor. The wind is moving from the left to the right of the figures. The dashed circle represents observers at a distance equal to the sum of the wind turbine height and the wind turbine rotor radius, that is, 124 m, of which the downwind position is defined in IEC 64100-11 as the standard observer.

The noise footprint in Figures 20–23 is dependent on the noise directivities exemplified in Figures 15 and 18 and the blade's pitch angle, θ. The trailing-edge noise maxima of the directivity lobes in Figure 15 are at $\phi - \theta = 147°$ and $\phi - \theta = 208°$, or namely, much of the sound pressure is directed towards the ground during the downward motion of the blade. Hence, the footprint is distributed almost symmetrically between the rotor plane in Figures 20B–23B, and it is further skewed due to the blade's pitch angle. In contrast, the maxima of the slat noise in Figure 18 are at $\phi - \theta = 135°$ and $\phi - \theta = 245°$. Accounting for the slat's pitch angle, the same angle at the lower lobe in Figure 18A is directed upwind, whereas at the upper lobe, it is directed to the ground. Hence, the noise footprint of the slat noise is farther from the rotor plane in the upwind than in the downwind direction.

The noise footprint shows a distinct jump upwind and downwind of the rotor plane in Figure 20A. In addition to the reason given above, the difference of level can be caused by the difference of the sound pressure maxima of the two halves of the noise directivity lobes. This is less observed in the other cases, because the sound pressure maxima of the two halves of the noise directivity is approximately equal. Furthermore, the sound pressure of $U_0 = 4$ m/s case in Figure 18 is much lower than the other cases, which result in a lower noise footprint.

At the standardized observer location, the contribution of the slat noise and the outboard trailing-edge noise is shown by the A-rated overall sound pressure level (L_p, dBA) in Figure 24. With increasing wind speeds, the slat noise level increases more rapidly than the outboard trailing-edge noise, such that the slat noise is louder than the outboard trailing-edge noise for $U_0 = 16$ m/s. Note that slat noise contributions are
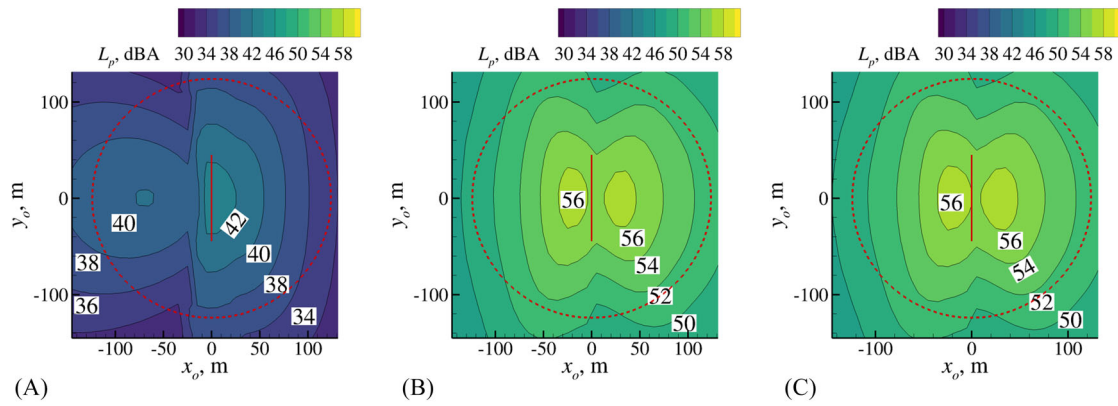
FIGURE 21 With $U_0 = 6$ m/s, the noise footprint for one revolution from (A) slat, (B) outboard trailing edge, and (C) combination of both
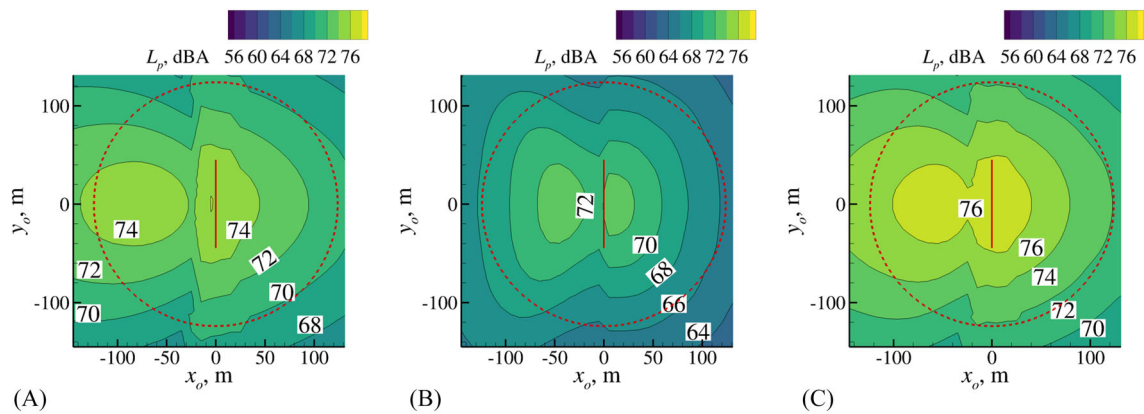

FIGURE 22 With $U_0 = 9$ m/s, the noise footprint for one revolution from (A) slat, (B) outboard trailing edge, and (C) combination of both
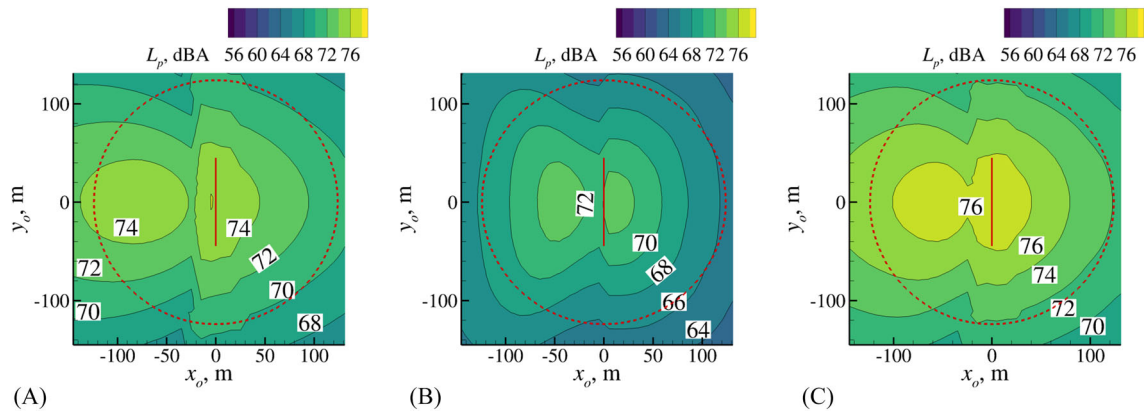

FIGURE 23 With $U_0 = 16$ m/s, the noise footprint for one revolution from (A) slat, (B) outboard trailing edge, and (C) combination of both

negligible only for the lowest wind speed $U_0 = 4$ m/s. In contrast, the overall sound pressure levels are increasingly affected by the slat's presence at the higher wind speeds.

Figure 25 shows the overall sound pressure level of each U_0 to Θ, the angle the ground observer is facing the wind turbine. In this figure, $\Theta = 0°$ indicates the downwind position, and Θ increases in the counter-clockwise direction of the circle in Figure 20. The observer remains at the standard distance of 124 m from the wind turbine.
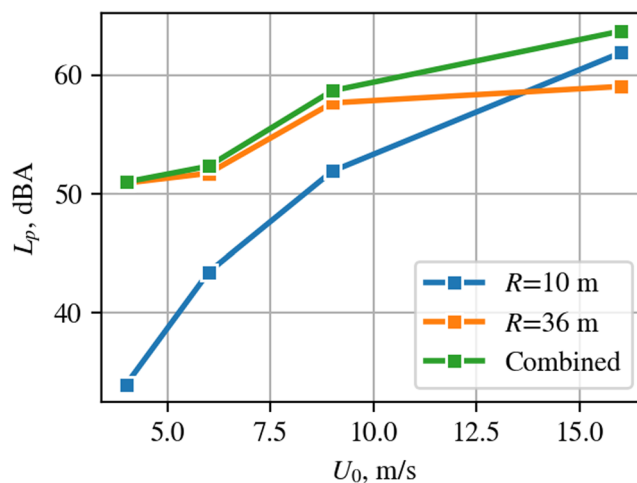
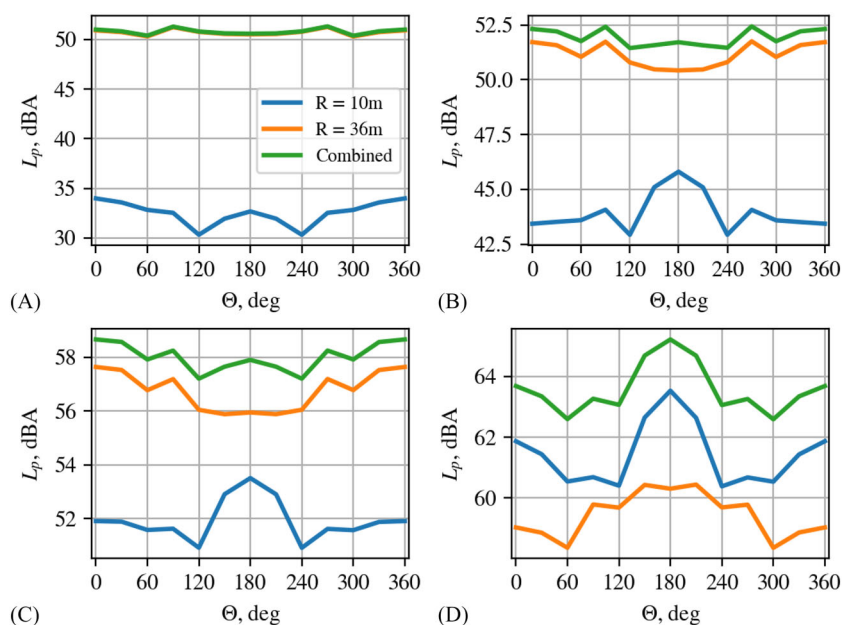**FIGURE 24** A-rated overall sound pressure level versus wind speed, U_0

FIGURE 25 A-rated overall sound pressure levels with respect to the azimuth angle, Θ: (A) $U_0 = 4$ m/s, (B) $U_0 = 6$ m/s, (C) $U_0 = 9$ m/s, and (D) $U_0 = 16$ m/s

At $U_0 = 4$ m/s, see Figure 25A, the low slat noise level gives approximately 17 dB less than the outboard trailing-edge noise. At $U_0 = 6$ m/s and $U_0 = 9$ m˙/s, the slat contributes to an additional 0.5–1 and 1–2 dBA, respectively. The slat noise is maximum upwind of the wind turbine; however, the outboard trailing edge remains to be the predominant sound source with its maximum radiation downwind of the wind turbine. One can also observe two local noise peaks at $\Theta = 90°$ and $270°$, or along the rotor plane.

For 6 m/s $\leq U_0 \leq 9$ m/s, see Figure 25B,C, the maximum radiation of the slat noise is upwind of the wind turbine, whereas the outboard trailing-edge noise is maximum directly downwind of the wind turbine. The combined sound sources are predominated by the outboard trailing-edge noise. The slat noise contribution to the total is negligible for $U_0 = 4$ m/s. For $U_0 = 6$ m/s and $U_0 = 9$ m/s, the slat contributes to an additional 0.5–1 and 1–2 dBA, respectively.

At $U_0 = 16$ m/s, shown in Figure 25D, the slat noise is louder than the trailing-edge noise at all Θ. Furthermore, the combined source's maximum noise level is upwind of the wind turbine, similar to the slat noise. The difference of overall sound pressure levels at the upwind and downwind at $U_0 = 16$ m/s is approximately 1.5 dBA. However, this wind speed can be considered as an *off-design* condition, because the blade is in the fully loaded region for $U_0 \geq 12$ m/s, and on-site, this wind speed is rarely achieved.[27]

6 | CONCLUSIONS

Three-dimensional aeroacoustic simulations based on a volume of the flow around much of the trailing edge and the flap-side edge show good agreement with the sound pressure level measured in the acoustic wind tunnel, AWB. Furthermore, a numerical analysis localized at the flap side edge also show good agreement with the measured data. These comparisons served to validate the numerical prediction using FRPM/FMCAS to predict an arbitrary radiating edge.

The prediction method was then applied to sections of a Suzlon S88 rotor blade, with blade length $\mathbb{R} = 44.45$ m, to rank the slat noise trailing edge and the outboard trailing edge. The findings are summarized below

1. FRPM/FMCAS simulation captured the trailing-edge noise and slat noise characteristics as determined from their respective scaling relations.
2. There is good agreement between the three-dimensional FMCAS results of a straight trailing edge and the two-dimensional PIANO results.
3. The maximum radiation of the outboard trailing-edge noise has a directivity angle on the lower lobe at a directivity angle of $208°$ + the blade's pitch angle.
4. The radiation maxima of the slat noise exist at the upper and lower lobes. The upper lobe maximum is at the directivity angle of $135°$ + the slat's pitch angle, and the lower lobe maximum is at the directivity angle of $245°$ + the slat's pitch angle.
5. By comparing the A-rated overall sound pressure levels, the sound emanating from 1 m span sections of the outboard rotor represented by the profile at $R = 36$ m is stronger than that emanating from the slat trailing edge represented by $R = 10$ m with the same span length for $-1.5° \leq \theta_p \leq 1.5°$.
6. The slat noise at higher wind speed of $U_0 = 16$ m/s is larger for all directivity angles ϕ, except for a narrow range of $204° < \phi < 246°$.

The acoustic of the rigid inboard slat and the outboard trailing edge at various ground positions 124 m away from the wind turbine's hub was evaluated using a fast and simple, non-empirical method. The method uses the noise calculation of a static model by FRPM/FMCAS to emulate the wind turbine blade's rotating conditions. The slat noise contribution to the combined noise source is negligible at $U_0 = 4$ m/s. The slat noise adds 1 dBA to the outboard trailing-edge noise at $U_0 = 9$ m/s. Slat noise levels at $U_0 = 16$ m/s are higher compared to the outboard trailing-edge noise; however, this wind speed is off-design, because the blades are fully loaded at $U_0 \geq 12$ m/s.

The advantage of FRPM/FMCAS is that the Helmholtz equation is resolved along the far-field boundary. Hence, scaling up the problem does not require as much resource as resolving a volumetric domain. The method presented also allows for the acoustic evaluation of wind turbine blades with additional blade elements, such as active trailing edges or rigid slats, discussed in this study. Furthermore, using the emulation method, the wind turbine noise at an arbitrary position can be calculated quickly. Although not performed here, a full-scale analysis of a blade is possible. As such, the tools presented in this work can be used to design low-noise wind turbines efficiently. A key aspect of our upcoming research will be the application of the noise prediction method for a real wind turbine in comparison to free-field measurements to validate the method for a full-scale wind turbine.

PEER REVIEW
The peer review history for this article is available at https://publons.com/publon/10.1002/we.2784.

DATA AVAILABILITY STATEMENT
Blade geometry data are subject to third-party restrictions. Other data are available on request from the authors.

ORCID
Alexandre Suryadi https://orcid.org/0000-0002-5129-5510
Florian Nils Schmidt https://orcid.org/0000-0002-5537-7214

REFERENCES
1. LI B, Jones WH, Lio JA. Rossiter, Overcoming fundamental limitations of wind turbine individual blade pitch control with inflow sensors. *Wind Energy*. 2018;21(10):922-936.
2. Oerlemans S, Schepers JG. Prediction of wind turbine noise and validation against experiment. *Int J Aeroacoust*. 2009;8(6):555-584.

3. Wasala SH, Storey RC, Norris SE, Cater JE. Aeroacoustic noise prediction for wind turbines using large eddy simulation. *J Wind Eng Ind Aerodyn*. 2015; 145:17-29.

4. Lau ASH, Kim JW, Hurault J, Vronsky T. A study on the prediction of aerofoil trailing-edge noise for wind-turbine applications. *Wind Energy*. 2017; 20(2):233-252.

5. Brooks TF, Pope DS, Marcolini MA. Airfoil self-noise and prediction. *Technical Report*, NASA Reference Publication 1218, National Aeronautics and Space Administration; 1989.

6. Lummer M, Akkermans RA, Richter C, Pröber C, Delfs J. Validation of a model for open rotor noise predictions and calculation of shielding effects using a fast BEM. In: 19th AIAA/CEAS Aeroacoustics Conference, Berlin, Germany. American Institute of Aeronautics and Astronautics; 2013.

7. Ewert R. Broadband slat noise prediction based on CAA and stochastic sound sources from a fast random particle-mesh (RPM) method. *Comput Fluids*. 2008;37(4):369-387.

8. Ewert R, Dierke J, Siebert J, et al. CAA broadband noise prediction for aeroacoustic design. *J Sound Vib*. 2011;330(17):4139-4160.

9. Reiche N, Ewert R, Delfs J. Realization of arbitrary vorticity spectra using generic stochastic turbulence. In: 22nd AIAA/CEAS Aeroacoustics Conference, Lyon, France. American Institute of Aeronautics and Astronautics; 2016.

10. Reiche N, Ewert R, Lummer M, Delfs J. Fast multipole boundary element method with stochastic sources for broadband noise simulation. In: 23rd AIAA/CEAS Aeroacoustics Conference, Denver, Colorado. American Institute of Aeronautics and Astronautics; 2017.

11. Gorski JJ, Bernard PS. Modeling of the turbulent enstrophy equation. *Int J Eng Sci*. 1996;34(6):699-714.

12. Launder BE, Sharma BI. Application of the energy-dissipation model of turbulence to the calculation of flow near a spinning disc. *Lett Heat Mass Transfer*. 1974;1(2):131-137.

13. Reiche N, Lummer M, Ewert R, Delfs JW. *Synthetic Turbulence Imposed as Boundary Condition for Fast Multipole BEM*: Waves Vienna; 2019.

14. Suryadi A, Jätz C, Herr M, Seume J. Identifying the flap side-edge noise contribution of a wind turbine blade section with an active trailing-edge. *Wind Energy*. 2021.

15. Sijtsma P. CLEAN based on spatial source coherence. *Int J Aeroacoust*. 2007;6(4):357-374.

16. Herr M, Rossignol K-S, Delfs J, Lippitz N, Mößner M. Specification of porous materials for low-noise trailing-edge applications. In: 20th AIAA/CEAS Aeroacoustics Conference, Atlanta, GA. American Institute of Aeronautics and Astronautics; 2014.

17. Showkat Ali SA, Szoke M, Azarpeyvand M, Ilario da Silva CR. Turbulent flow interaction with porous surfaces. In: 2018 AIAA/CEAS Aeroacoustics Conference, Atlanta, Georgia. American Institute of Aeronautics and Astronautics; 2018.

18. Rossignol K-S, Suryadi A, Herr M, Schmidt J, Tychsen J. Experimental investigation of porous materials for trailing-edge noise reduction. *Int J Aeroacoust*. 2020;19(6-8):365-384.

19. Herr M. Experimental study on noise reduction through trailing edge brushes. In: Hirschel EH, Schröder W, Fujii K, Haase W, Leer B, Leschziner MA, Pandolfi M, Periaux J, Rizzi A, Roux B, Rath H-J, Holze C, Heinemann H-J, Henke R, Hönlinger H, eds. *New Results in Numerical and Experimental Fluid Mechanics V*, Vol. 92: Springer Berlin Heidelberg; 2006:365-372.

20. Suryadi A, Martens S, Herr M. Trailing edge noise reduction technologies for applications in wind energy. In: 23rd AIAA/CEAS Aeroacoustics Conference, Denver, Colorado. American Institute of Aeronautics and Astronautics; 2017.

21. Rautmann C. Generic airfoil trailing-edge noise prediction using stochastic sound sources from synthetic turbulence. In: 20th AIAA/CEAS Aeroacoustics Conference, page 21, Atlanta, Georgia. AIAA; 2014.

22. Wohlbrandt A, Hu N, Guérin S, Ewert R. Analytical reconstruction of isotropic turbulence spectra based on the Gaussian transform. *Comput Fluids*. 2016;132:46-50.

23. Reiche N, Lummer M, Ewert R, Delfs JW. Anisotropic synthetic turbulence and fast multipole BEM for high-lift noise prediction. Numerical Methods 19; 2015.

24. Brooks TF, Humphreys Jr. WM. Flap-edge aeroacoustic measurements and predictions. *J Sound Vib*. 2003;261:31-74.

25. Oerlemans S, Fisher M, Maeder T, Kögler K. Reduction of wind turbine noise using optimized airfoils and trailing-edge serrations. *AIAA J*. 2009;47(6): 1470-1481.

26. Jaume AM, Wild J. Aerodynamic design and optimization of a high-lift device for a wind turbine airfoil. *New Results in Numerical and Experimental Fluid Mechanics X*, Vol. 132: Springer International Publishing; 2016:859-869.

27. Schmidt FN, Wild J. Technical Report 3.3.4.4, Bericht zur aerodynamischen Wirksamkeit des Vorflügels auf realer WEA [Report on the aerodynamic effectiveness of the slat on a full-scale wind turbine]. *SmartBlades2—Bau, Test und Weiterentwicklung Intelligenter Rotorblätter, Köln*: DLR Deutsches Zentrum für Luft- und Raumfahrt e.V; 2021. [In German].

28. Schwamborn D, Gerhold T, Kessler R. DLR-TAU Code—an overview. In: 1st ONERA/DLR Aerospace Symposium, Paris; 1999:S4-2–S4-10.

29. Oerlemans S, Fisher M, Maeder T, Kögler K. Reduction of wind turbine noise using optimized airfoils and trailing-edge serrations. *AIAA J*. 2009;47(6): 1470-1481.

30. Dobrzynski W, Pott-Polle M. Slat noise source studies for farfield noise prediction. In: 7th AIAA/CEAS Aeroacoustics Conference and Exhibit, Maastricht, Netherlands. American Institute of Aeronautics and Astronautics; 2001.

31. Appel C, Fassmann B, Lin S-Y, Herr M. CAA-basierte Schallvorhersage für Windkraftanlagen [CAA-based sound prediction for wind turbines]. In: Fortschritte der Akustik—DAGA 2020, Tagungsband DAGA, page 4, Hannover. Deutsche Gesellschaft für Akustik e.V.; 2020. [In German].